Research Square

Preprints are preliminary reports that have not undergone peer review.
They should not be considered conclusive, used to inform clinical practice,
or referenced by the media as validated information.

Policy-driven winter-to-spring emissions shift enhances oxidizing capacity in China

Fei Jiang

jiangf@nju.edu.cn

Nanjing University https://orcid.org/0000-0003-1744-7565

Mengwei Jia

Nanjing University

Xin Huang

Nanjing University https://orcid.org/0000-0003-0922-5014

Zilin Wang

Nanjing University

Nikolaos Evangeliou

Norwegian Institute for Air Research https://orcid.org/0000-0001-7196-1018

Nan Wang

Sichuan University

Shuzhuang Feng

Nanjing University

Tianliang Zhao

Nanjing University of Information Science and Technology

Lian Xue

Nanjing University

Yuning Xie

Guangxi Zhuang Autonomous Region Ecological and Environmental Monitoring Centre

Runxi Pan

Guangxi Zhuang Autonomous Region Ecological and Environmental Monitoring Centre

Weimin Ju

Nanjing University https://orcid.org/0000-0002-0010-7401

Aijun Ding

Nanjing University https://orcid.org/0000-0003-4481-5386

Article

Keywords:

Posted Date: June 4th, 2026

DOI: https://doi.org/10.21203/rs.3.rs-9871669/v1

License: This work is licensed under a Creative Commons Attribution 4.0 International License.
Read Full License

Additional Declarations: There is **NO** Competing Interest.

Abstract

Atmospheric oxidizing capacity (AOC) critically drives the formation of secondary air pollutants, which impose great health and ecosystem risks in spring. Yet many studies have investigated annual, winter, or summer AOC in China, leaving the evolution of springtime AOC and its underlying drivers unclear. Here we combine ground-based and satellite observations to analyze AOC dynamics in China from 2014 to 2019 and quantify its underlying drivers using high-resolution anthropogenic emissions inferred from nationwide in-situ observations. We identify a pronounced increase in springtime AOC after 2017, along with a marked seasonal shift in emissions from winter to spring. Numerical simulations show that neither meteorology nor emission inventory variations can explain this enhancement, whereas incorporating the seasonal emission shift explains approximately 74% of the observed national AOC increase. This shift is directly attributable to China's winter focused clean air policies implemented since late 2016, which rigidly curtailed industrial production from November 15 to March 15 and triggered a sharp spring rebound. Our findings underscore the urgent need to refine seasonal allocation in emission inventories and suggest that future air quality management should account for the seasonal disparities in atmospheric oxidation and photochemical pollution.

Main

The atmosphere can oxidize, transform, and remove reduced trace gases and pollutants, a property known as atmospheric oxidizing capacity (AOC)[1,2]. While an appropriate level of AOC sustains the atmospheric self-cleansing ability, excessive oxidation may not only affect ozone (O_3) concentrations, but also accelerates the transformation of sulfur dioxide (SO_2), nitrogen oxides (NO_x), and volatile organic compounds (VOCs) into sulfate, nitrate, and secondary organic aerosols[3-6]. AOC intensify photochemical pollution and degrade air quality, with substantial impacts on human health, forest ecosystems, and crop productivity[7]. These impacts underscore the importance of understanding the temporal evolution of AOC and its underlying drivers.

In China, a series of emission control policies implemented over the past decade (Phase I: 2013-2017; Phase II: 2018-2020; Phase III: 2023-2025)[8-10] have substantially reduced primary pollutants, yet surface O_3 has continued to rise[11,12]. This apparent contradiction highlights the strongly nonlinear response of air quality to emissions and has shifted attention towards AOC[13]. Numerous studies have demonstrated that surface O_3 peaks across many regions in China have shifted from summer to spring[14-19], creating conditions conducive to an earlier onset of compound air pollution[11,12]. Meanwhile, spring is characterized by increased outdoor human activity and rapid vegetation growth with fully open stomata, factors that not only raise human exposure and vegetation uptake of pollutants but also coincide with a period when human immune systems are more sensitive and young leaves are more vulnerable to pollution damage. These factors lead to a synergistic amplification, making the health and ecological impacts of AOC-driven pollution in spring substantially more severe than in other seasons[20,21].

Existing AOC studies in China have focused primarily on annual scale or on winter and summer, as winter pollution is typically most severe and summer has the strongest photochemistry. Accordingly, numerous studies have conducted field measurements or applied box models during these seasons to investigate chemical mechanisms governing AOC and identify key species that modulate its intensity[5,22-26]. Chemical transport models have been used to perform emission-sensitivity experiments to quantify the contributions of meteorology and emissions to AOC variability[11,16,18,19,23]. However, emission inventories driving these models have substantial spatiotemporal uncertainties, particularly during rapid policy-driven emission changes[27,28]. Moreover, the response of AOC to emissions is highly nonlinear, posing challenges for interpreting AOC variations within existing inventories[15]. For spring, although surface ozone has shown a persistent increase in recent years[11,12,29], implying intensified atmospheric oxidation processes[14,30], there remains a lack of clear characterization of springtime AOC trends and a mechanistic understanding of the driving processes.

To elucidate the spatiotemporal evolution of springtime AOC in China and the physicochemical mechanisms under sustained emission controls, we conducted the following analyses. First, we characterized springtime AOC evolution using both ground-based and satellite measurements. Second, we integrated monthly anthropogenic emission inversions with a mesoscale chemical transport model to quantify the relative contributions of meteorology and springtime emissions to AOC. Finally, we clarified the mechanisms underlying the springtime AOC in China. Together, our results provide a comprehensive framework for understanding the characteristics, drivers, and mechanisms of springtime AOC changes in China during the emission control period.

Enhanced atmospheric oxidation in spring

Since 2013, the monitoring network of China's Ministry of Ecology and Environment (MEE) has continuously measured six atmospheric pollutants, including reactive species such as NO_2 and O_3, and relatively stable species like carbon monoxide (CO) and $PM_{2.5}$. Interannual variations from 2014 to 2019 (Figure S1) show that sustained emission control policies have led to year-round declines in CO and $PM_{2.5}$. In contrast, O_3 has continued to rise, most notably in spring (March - May).

In aerosol-rich environments, the sum of NO_2 and O_3 concentrations (O_x,i.e., $O_3 + NO_2$) is a widely used as a proxy of AOC and photochemical activity[31,32], because it captures multiphase oxidation processes and reduce NO titration effects. Compared with OH, O_x is more readily observed, making it more suitable for large-scale and long-term AOC analyses. Seasonal mean O_x concentrations indicate that AOC in China peaks in spring rather than summer (Figure S1). Trend analysis reveals the strongest increase in spring AOC, while winter (last December - February) is the only season with a declining trend. Notably, spring O_x has increased markedly since 2017, with national mean concentrations rising from 51.0 ± 0.7 ppb (2014-2016) to 54.6 ± 0.5 ppb (2017-2019). During 2017-2019, approximately 70.0% of monitoring sites recorded higher spring O_x than in 2014-2016 (Figure 1 and Figure S2).

Formaldehyde (HCHO) vertical column densities (VCD), observed by the Ozone Monitoring Instrument (OMI) on NASA's Aura satellite, were widely used as an indicator of photochemical activity and VOC oxidation[33]. As a reactive intermediate in VOCs oxidation and a HO_x radical source, HCHO VCD correlates with OH reactivity and photochemical activity[34,35]. To minimize biogenic VOC influences and isolate anthropogenic signals, we focus on HCHO VCD at the locations with national monitoring sites, typically located in urban areas. Spring HCHO VCD increased from 8.4 (± 0.1) × 10^{15} molecules cm^{-2} (2014-2016) to 9.0 (± 0.2) × 10^{15} molecules cm^{-2} (2017-2019), with 68.3% of stations exhibiting rises (Figure 1 and Figure S2).

Seasonal shift of anthropogenic emissions

Both anthropogenic and natural emissions can influence AOC. Without extreme climate anomalies, natural emissions contribute little to interannual variability compared with anthropogenic sources[36]. Surface O_x and satellite HCHO VCD observations are spatially concentrated over urban centers, indicating that the observed AOC enhancement primarily reflects intensive human activity. Exploring its drivers requires high-precision data capturing human activity. CO is predominantly emitted from incomplete combustion associated with transportation, industrial processes, and residential energy use, which closely reflects anthropogenic activity across China[37-39]. With a well-constrained OH sink and a lifetime of one to three months, CO is widely accepted as a robust tracer of primary anthropogenic emissions[34]. However, current CO emission inventories for China remain highly uncertain, with reported differences reaching several-fold[27,28]. This motivates a top-down inversion approach to better constrain CO emissions and their seasonal variability.

In a previous study, we quantified anthropogenic CO emissions over China at 0.2° × 0.2° resolution, revealing strong interannual variability and spatial heterogeneity[40]. Seasonal analysis of monthly CO inversions for 2014-2019 shows patterns differing substantially from the bottom-up inventory (Figure 2). In current inventories, monthly CO profiles are fixed and highly regular, unlikely to capture realistic variability (Figure S3). Not only CO but also the emissions of key AOC precursors, NOx and NMVOCs, show nearly invariant monthly profiles in the original inventory from 2014-2019. Such weak temporal variability contrasts sharply with the substantial changes in emission control and anthropogenic activities across China during this period, implying that the inventory may not fully capture actual seasonal redistribution. From inverted CO emissions (Figure 2), we find that summer and autumn contributions remain stable, while emissions shift from winter to spring. During 2014-2016, winter had the highest anthropogenic CO emissions in China, followed by spring. In contrast, after 2017, springtime emissions exceeded winter emissions.

Spatial analysis (Figure 2) shows that during 2017-2019, more than 64.7% of mainland China experienced higher spring than winter emissions, versus only 38.2% in 2014-2016. This shift was most pronounced in densely populated, economically developed regions with high baseline emissions, including the Beijing-Tianjin-Hebei (BTH), Yangtze River Delta (YRD), and Pearl River Delta (PRD) (Figure

S4). The top GDP-ranked city in Hebei, Tangshan, exhibited a notable shift. In YRD, the shift was prominent along the Yangtze River Economic Belt. In PRD, it intensified in Shenzhen, Dongguan and Huizhou, both among the province's five largest economies. However, the emission shift was not uniform, for example, the Fenwei Plain (FWP) showed no clear seasonal shift - emissions increased during the Phase I of emission reduction policies[41], then it was designated a key region in the Phase II[9], explaining the absence of seasonal shift there.

Emission seasonal shift boosts spring oxidation

To investigate the underlying mechanisms of the enhanced springtime AOC, we use the regional air quality model Weather Research and Forecasting Model coupled with Chemistry (WRF-Chem)[42] to simulate atmospheric oxidation under varying meteorological conditions and emission scenarios. We focused on springs of 2014 and 2017 as representative periods, corresponding to the first year following the initiation of Phase I and its final year, respectively. A series of sensitivity experiments was conducted (See Methods and Table S2) to quantify the effects of changes in meteorological conditions and in emissions without and with seasonal shifts on AOC. The emission changes without seasonal shifts were directly from the emission inventory of Multi-resolution Emission Inventory model for Climate and air pollution research (MEIC) v1.4[43] (Figure S3). For emissions with seasonal shifts, since it is difficult to obtain data on the seasonal emission shift profiles in species related to changes in AOC, primarily NO_x and NMVOC, we assume that their seasonal shift profiles are the same as those for CO, as described in the above section. This assumption is justified because the emissions of these species are mainly from combustion-related sources, which to a large extent are the same as those for CO.

Compared with spring 2014, the observed O_x in spring 2017 increased markedly across most Chinese cities, especially in eastern regions (Figure 3a). When considering only meteorological differences between the two springs, the simulated O_x levels in 2017 showed a pronounced decline across all regions of China except in the southern provinces of Guangdong, Guangxi, Yunnan, and Fujian, where increases occurred. The strongest decreases were in Shanxi and Hebei (Figure 3b). These results indicate that meteorological conditions primarily suppressed springtime O_x in 2017. When further accounting for anthropogenic emission changes without seasonal shifts, O_x levels decreased even more relative to 2014, with the declines becoming more widespread and intense. This is mainly because, without seasonal shifts, the emissions estimated in the inventory for spring 2017 were lower than those for spring 2014 across all regions of China (Figure S3), leading to further weakened O_x levels (Figure 3c and Figure S6). Finally, when seasonal emission shifts were included, the simulated O_x concentrations reversed to widespread increases, and the spatial pattern of simulated O_x changes became similar to the observed results (Figure 3d), clearly demonstrating that seasonal emission shifts dominated the enhanced springtime AOC.

We further quantified the contributions to observed O_x changes across six regions (i.e., East, North, Northeast, Northwest, Southwest, and South-Central China; Figure 3e). The observed increases ranged

from 2.6 to 4.1 ppb, with a national average of 3.6 ppb. Considering only meteorological changes, simulations gave a national decrease of −0.5 ppb, with the strongest suppression in North China (−3.2 ppb) and increases only in East China (0.3 ppb) and South-Central China (1.2 ppb). Adding emission changes without seasonal shifts further reduced O_x by about 1 ppb per region, dropping the national mean from −0.5 to −1.7 ppb. Including seasonal emission shifts then reversed the national mean to an increase of 2.7 ppb, with simulated regional O_x increases comparable to the observed values, especially in Northeast, East, South-Central, and Southwest China. Overall, the seasonal emission shifts explain 74.1% of the observed enhancement.

Discussions and Implications

We reveal a pronounced increase in springtime AOC in China after 2017, along with a clear shift in emissions from winter to spring, i.e., reduced winter emissions alongside increased spring emissions. Previous studies have highlighted the influences of meteorological variability, aerosol-radiation interactions by $PM_{2.5}$ reductions, and changes in precursor emissions from emission inventories on atmospheric oxidation and O_3 pollution[11,12,17,44]. However, we find that when only meteorological changes and inventory-based emission changes are considered, simulated springtime AOC decreases rather than increases, meaning that these factors cannot explain the observed increase. Although reduced $PM_{2.5}$ could theoretically enhance AOC by increasing photolysis rates, our simulations fully account for these radiative effects (see Method), suggesting they are not the primary driver. In contrast, when we additionally consider the seasonal emission shift, the simulated AOC increases notably and explains up to 74% of the observed enhancement, indicating that the shift is the main driver of the increased AOC.

The seasonal emission shift is directly attributable to China's winter-focused clean air policies. While winter has traditionally been the most polluted season, the late 2016 policy[45] marked a decisive turning point in the regulatory approach. The October 2016 notice[45] was the first to systematically mandate exact staggered production timelines from November 15 to March 15 for key industries including cement, power plants, casting, and brick kilns, extending the "flexible maintenance scheduling" in the 2015 notice (MEE Doc. No. 101)[46] into a rigid system. This schedule suppressed winter emissions across the 2016-2017 heating season and has been institutionalized. For instance, the 2018-2019 BTH action plan[47] retained the same start date and emphasized that "staggered production lists, once finalized, shall not be arbitrarily adjusted." However, this rigid timeline also triggered a sharp and systematic springtime production rebound. Industrial emissions surged immediately after the staggered production period ended. Real-time online monitoring across the "2+26" cities showed that average SO_2 and NO_x emissions in late-March of 2018 increased by 10% and 30%, respectively, compared to the first half of the same month, with the largest increases in the steel and cement sectors[48]. Ground-based atmospheric observations in Beijing further confirm the resumption of industrial activities after the staggered production period, as evidenced by a pronounced rebound in CO that nearly doubles

compared to the staggered production period[49]. Industrial activity indicators also show widespread springtime increases after 2017 (Figure S9)[50-57]. In addition, a previous study noted that wintertime air pollution control produces a short-term “policy-induced blue sky” follows by “retaliatory pollution” after the control ends[58].

Given more favorable meteorological condition for photochemistry in spring, the same emissions produce stronger oxidation and secondary pollution. Our results indicate that seasonally shifted emissions alter oxidation pathways by increasing springtime NO_x, VOCs, and CO emissions, thereby changing oxidation-related species, including O_3, NO_3 radicals, N_2O_5, and particulate nitrate (Figure 4, Figure S7 - S8). This enhancement exhibits clear regional differences and aligns well with the NO_x-limited and VOC-limited regimes in China[59-61]. In northern VOC-limited regions, higher NO_2 suppresses OH through radical termination, limiting daytime O_3 production, but also accelerates nighttime NO_3-N_2O_5 conversion and N_2O_5 hydrolysis, promoting rapid NO_x oxidation into nitrate. This mechanism helps explain the post-2017 increases in nitrate and the shift of heavy pollution episodes from winter to spring in northern China[62-64]. In southern NO_x-limited regions, seasonal emission shifts alone can increase O_3, differing from previous explanations emphasizing NO_x reductions, $PM_{2.5}$ declines, and meteorological changes[17-19]. Overall, the seasonal emission shift enhances both daytime photochemistry and nighttime nitrogen oxidation, strengthening AOC and promoting secondary pollution formation.

Nevertheless, this study has several limitations. First, uncertainties in meteorological simulations may affect O_x through biases in temperature and wind fields, although comparable model performance between spring 2014 and 2017 (Table S1) suggests reasonably consistent interannual differences (see Supplementary Text for more details). Second, emission inventories remain uncertain. Previous studies[27,40] confirmed larger uncertainties in Northwest China, partly explaining discrepancies between simulated and observed O_x enhancements even after considering the emission shift. Third, unlike combustion-dominated CO and NO_x emissions, NMVOCs originate from diverse non-combustion sources (e.g., solvent use, industrial processes, and oil and gas evaporation)[65]. Assuming the same seasonal shift profile for NMVOCs as CO may bias simulated AOC, particularly in VOC-limited North China[66]. Fourth, the seasonal emission shift framework does not include methane, SO_2, or primary $PM_{2.5}$, which can influence AOC through OH loss[67] or aerosol–radiation interactions[68,69]; however, their effects are generally secondary compared with CO, NO_x, and NMVOCs.

In summary, our results demonstrate the recent increase in springtime AOC, driven jointly by seasonally shifted emissions and nonlinear chemistry. These findings reveal a critical blind spot in current air quality management: strategies focused on annual means or wintertime peaks may inadvertently create seasonal vulnerabilities, underestimating springtime photochemical pollution and facilitating earlier O_3 and secondary aerosol formation. Our results highlight the need for seasonally differentiated control strategies to mitigate adverse impacts on human and ecosystems. More broadly, observation-

constrained emission inversions offer a more dynamic, policy-relevant representation of emission changes, improving understanding of AOC variability and supporting adaptive air quality management.

Method

Atmospheric oxidation capacity observations

We characterized variations in AOC using both ground-based observations and satellite remote sensing. Ambient O_x concentrations were calculated from hourly ground-based observations of NO_2 and O_3 from approximately 1,600 monitoring stations across China, operated by the MEE, during 2014-2019. Atmospheric NO_2 and O_3 observations followed the National Environmental Protection Standards[70-72]. Monitoring instruments were operated continuously under controlled conditions (temperature: 25 ± 5 °C; relative humidity < 80%) and were subject to routine maintenance, cleaning, and calibration to ensure data quality. All data were obtained from the MEE data platform.

We used total column HCHO data observed by the Ozone Monitoring Instrument (OMI) from the NASA Goddard Earth Sciences Data and Information Services Center[73]. The OMI sensor is on board the Aura satellite, with a swath width of 2,600 km and a spatial resolution of 13 km × 24 km, providing global coverage once per day. The HCHO total column data were resampled to a spatial resolution of 0.1° × 0.1°. Only data with good quality were retained (qa_statistics_data_quality_flag = 0 and 1). Seasonal mean HCHO column concentrations for spring and winter during 2014-2019 were then calculated.

Anthropogenic CO emissions constrained by *in-situ* observations

The study utilizes a high-resolution dataset of anthropogenic CO emissions over China for 2014–2019, with a spatial resolution of 0.2° × 0.2° and monthly temporal resolution40. The dataset was derived using a top-down approach constrained by CO concentrations observed from over 1600 national air quality monitoring stations in China, providing extensive spatial coverage and robust observational constraints.

The inversion was performed with the Lagrangian atmospheric transport model FLEXPART (v10.1)[74], combined with the Bayesian inversion framework FLEXINVERT[75]. Backward trajectory simulations were conducted to quantify source–receptor relationships, while background CO concentrations from global reanalysis were incorporated to account for long-range transport. Chemical loss of CO due to reactions with OH was explicitly considered using prescribed monthly OH fields. By integrating transport, background concentrations, and chemical processes, the inversion establishes a physically consistent relationship between emissions and observations, thereby effectively capturing the spatiotemporal variability of anthropogenic CO emissions.

Regional air quality model and model configuration

To investigate the impact of emission shifts on AOC, we employed WRF-Chem V3.9[42]to simulate AOC over China under different emissions and meteorological scenarios. The WRF-Chem model can account

for complex physical and chemical processes such as the emission and deposition of pollutants, convection and diffusion, gaseous and aqueous-phase chemical transformations, and aerosol chemistry and dynamics. The simulations were conducted for spring (March–May) of 2014 and 2017 at a horizontal resolution of 27 km. Meteorological forcing for WRF-Chem was obtained from the NCEP Final Operational Global Analysis (FNL) dataset. A 48-hour spin-up period was applied, and the first 7 days of simulation were discarded to ensure adequate model spin-up and stabilization of chemical fields. We employed 33 vertical layers up to 100 hPa in the model, with enhanced resolution in the lower troposphere.

The chemical mechanism used in WRF-Chem was Carbon Bond Mechanism (CBMZ)[76], and the aerosol chemistry was treated with the Model for Simulating Aerosol Interactions and Chemistry (MOSAIC)[77]. We considered the feedback effects of aerosols on meteorological fields. Physical parameterizations included the Yonsei University boundary layer scheme (YSU)[78], the Grell-Freitas ensemble cumulus scheme[79], the Lin microphysics scheme[80], the RRTMG longwave and shortwave radiation schemes[81,82], the revised Monin-Obukhov surface layer scheme[83], and the Noah land surface model[84,85]. To improve meteorological accuracy, a Newtonian relaxation (nudging) technique was applied[86,87], assimilating three-dimensional meteorological observations every six hours. The nudging data were obtained from the National Centers for Environmental Prediction (NCEP) ADP Global Upper Air Weather Observations dataset, a comprehensive collection of global upper-air meteorological observations compiled by NCEP[88], providing observations at up to 20 vertical levels, including pressure, geopotential height, upper-air temperature, dew point temperature, upper-level winds, and surface wind fields from ground-based platforms.

Sensitivity experiment design

We designed four cases to assess the impacts of seasonal emission shifts, emission inventory changes, and meteorological variability, as summarized in Table S2. Case 1 simulates the O_x concentration field for March–May 2017 using the MEIC emission inventory and FNL meteorological fields for the same period to drive the WRF-Chem model. Case 2 is based on Case 1 but replaces the monthly emissions of species relevant to O_x with the monthly share of the CO emissions derived from the inversion. The modified species in Case 2 included CO, NO_x, and NMVOCs, with specific species listed in Table S3. For each grid cell, we calculated the monthly share of CO emission in both the original emission inventory and the inversion results. The annual total emissions of these species were then redistributed according to the monthly shares derived from the inversion to obtain the emission levels under the seasonal-shift scenarios. Figure S5 shows the mean monthly shares of the original and inverted emissions across all grid cells in 2017. The inverted emissions exhibit substantially higher monthly shares than the original inventory in April, May, and July, while their monthly shares are significantly lower in November, December, and January. The difference between Case 2 and Case 1 therefore isolates the impact of seasonal emission shifts on AOC; this experiment is referred to as SHIFT.

In addition to seasonal emission shifts, changes in the emission inventory itself are also important. Therefore, in Case 3, the emission inventory in Case 1 was replaced with the 2014 inventory. The difference between Case 3 and Case 1 represents the impact of emission inventory changes on O_x, and this experiment is referred to as EI. Furthermore, differences in meteorological conditions may also contribute to anomalies in O_x concentrations. In Case 4, the meteorological fields from Case 1 were replaced with those from 2014. The difference between Case 1 and Case 4 thus quantifies the contribution of meteorological differences between spring 2017 and spring 2014 to O_x concentrations; this experiment is referred to as METEO.

Acknowledgements

The work was funded by the National Natural Science Foundation of China (NSFC) (Grant 42377102, 42507157), the Joint Fund of the Zhejiang Provincial Natural Science Foundation of China (Grant LZJMZ24D050008), the Natural Science Foundation of Jiangsu Province (Grant BK20251193), and Jiangsu Provincial Science Fund for Distinguished Young Scholars (Grant BK20231530). We gratefully acknowledge Andreas Stohl, Sabine Eckhardt for their valuable support on the emission inversion. We would like to thank the Ministry of Ecology and Environment of the People's Republic of China for making the hourly surface CO concentration observations available, and the ECMWF for providing the operational meteorological analyses. We also thank the MEIC team for providing the CO emission inventory. Additionally, we are also grateful to the High-Performance Computing Center (HPCC) of Nanjing University for doing the numerical calculations on its blade cluster system.

Declarations

Data availability

The inverted CO emission data are available at https://doi.org/10.5281/zenodo.13623164. The hourly surface O_3 and NO_2 concentration observations are available at https://air.cnemc.cn:18007, last accessed: 04/06/2026. The total column HCHO data observed by the Ozone Monitoring Instrument are available at https://disc.gsfc.nasa.gov/, last accessed: 04/26/2026. The operational meteorological analyses from ECMWF are available at https://www.ecmwf.int/en/forecasts/dataset/operational-archive, last accessed: 04/06/2026. The MEIC CO emission inventory is available at http://www.meicmodel.org/, last accessed: 04/06/2026. The ground-based wind speed and temperature observations from the NCEI are available at https://www.ncei.noaa.gov/, last accessed: 04/06/2026. The meteorological data used for nudging from NCEP are available at https://gdex.ucar.edu/datasets/d351000/#!/, last accessed: 04/06/2026.

Code availability

All analyses were conducted using MATLAB R2023a and NCL 6.4.0. The WRF-Chem source code is available at https://www2.acom.ucar.edu/wrf-chem, last accessed: 04/06/2026. The code central to the

analyses in this paper is available at https://doi.org/10.5281/zenodo.20465301, last accessed: 05/31/2026.

Author contributions

M.J.: Methodology, Visualization, Writing original manuscript, Funding acquisition. **F.J.**: Conceptualization, Writing - Review & Editing, Funding acquisition. **X.H.**: Providing perspectives and conceptual advice. **Z.W.**: Methodology. **N.E.**: Writing - Review & Editing. **N.W.**: Methodology. **S.F.**: Methodology. **T.Z.**: Writing - Review & Editing. **L.X.**: Data collection. **Y.X.**: Writing - Review & Editing. **R.P.**: Data collection. **W.J.**: Supervision, Writing - Review & Editing. **A.D.**: Conceptualization, Project administration.

Competing interests

The authors declare that they have no known competing financial interests or personal relationships that could have appeared to influence the work reported in this paper.

References

1. Thompson, A. M. The oxidizing capacity of the Earth's atmosphere: Probable past and future changes. *Science* 256, 1157–1165 (1992).
2. Prinn, R. G. The cleansing capacity of the atmosphere. *Rev. Environ. Resour.* 28, 29–57 (2003).
3. Wang, J. et al. Fast sulfate formation from oxidation of SO_2 by NO_2 and HONO observed in Beijing haze. *Commun.* 11, 2844 (2020).
4. Srivastava, D. et al. Formation of secondary organic aerosols from anthropogenic precursors in laboratory studies. *npj Clim. Atmos. Sci.* 5, 22 (2022).
5. Fan, B. et al. Atmospheric oxidation capacity and its influence on secondary pollution during winter PM_5 haze episodes in Urumqi. *J. Environ. Sci.* 160, 468-480 (2025).
6. Zhao, D. et al. Effects of NO_x and SO_2 on the secondary organic aerosol formation from photooxidation of α-pinene and limonene, *Chem. Phys.* 18, 1611–1628 (2018).
7. Monks, P. S. et al. Tropospheric ozone and its precursors from the urban to the global scale: From air quality to short-lived climate forcer, *Chem. Phys.* 15, 8889–8973 (2015).
8. State Council of China. Air Pollution Prevention and Control Action Plan, Beijing (2013).
9. State Council of China. Three-Year Action Plan for Defending the Blue Sky, Beijing (2018).
10. State Council of China. Air Quality Continuous Improvement Action Plan, Beijing (2023).
11. Dai, J. et al. The atmospheric oxidizing capacity in China – Part 2: Sensitivity to emissions of primary pollutants. *Chem. Phys.* 24, 12943–12962 (2024).
12. Li, K. et al. Increases in surface ozone pollution in China from 2013 to 2019: Anthropogenic and meteorological influences. *Chem. Phys.* 20, 11423–11433 (2020).

13. Liu, Z. et al. Enhanced atmospheric oxidation and particle reductions driving changes to nitrate formation mechanisms across coastal and inland regions of north China. *Chem. Phys.* 25(15), 8719–8742 (2025).
14. Chen, S. et al. The trend of surface ozone in Beijing from 2013 to 2019: Indications of the persisting strong atmospheric oxidation capacity. *Environ.242*, 117801 (2020).
15. Tan, Z. et al. Governing atmospheric oxidation capacity is the key to synergistic air quality and climate gains. *One Earth9*(1), 101569 (2026).
16. Wang, C. et al. Sensitivity analysis of atmospheric oxidation capacity in Beijing based on the GRAPES-CUACE adjoint model. *Environ.* 299, 119641 (2023).
17. Liu, Y., & Wang, T. Worsening urban ozone pollution in China from 2013 to 2017–Part 1: The complex and varying roles of meteorology. *Chem. Phys.* 20(11), 6305–6321 (2020a).
18. Liu, Y., & Wang, T. Worsening urban ozone pollution in China from 2013 to 2017–Part 2: The effects of emission changes and implications for multi-pollutant control. *Chem. Phys.* 20(11), 6323–6337 (2020b).
19. Li, K. et al. Ozone pollution in the North China Plain spreading into the late-winter haze season. *Natl. Acad. Sci. U.S.A.*, 118(10), e2015797118 (2021).
20. Qu, W. et al. Delayed leaf green-up is associated with fine particulate air pollution in China, *Commun.16*(1), 3406 (2025).
21. Anenberg, S. C., Haines, S., Wang, E., Nassikas, N. & Kinney, P. L. Synergistic health effects of air pollution, temperature, and pollen exposure: a systematic review of epidemiological evidence, *Health*19(1), 130 (2020).
22. Wei, L. et al. An observation-based analysis of atmospheric oxidation capacity in Guangdong, China. *Environ.*318, 120260 (2024).
23. Liu, T. et al. Atmospheric oxidation capacity and ozone pollution mechanism in a coastal city of southeastern China: analysis of a typical photochemical episode by an observation-based model, *Chem. Phys.22*(3), 2173-2190 (2022).
24. Qian, H. et al. Anthropogenic Oxygenated Volatile Organic Compounds Dominate Atmospheric Oxidation Capacity and Ozone Production via Secondary Formation of Formaldehyde in the Urban Atmosphere, *ACS ES&T Air2*(6), 1033-1041 (2025).
25. Tan, Z. et al. Daytime atmospheric oxidation capacity in four Chinese megacities during the photochemically polluted season: a case study based on box model simulation, *Chem. Phys.19*(6), 3493-3513 (2019).
26. Wang, H. et al. Increased night-time oxidation over China despite widespread decrease across the globe, *Geosci.16*(3), 217-223 (2023).
27. Feng, S. et al. (2020), CO emissions inferred from surface CO observations over China in December 2013 and 2017. *Geophys. Res. Atmos.* 125, e2019JD032101.

28. Kong, L. et al. Changes of air pollutant emissions in China during two clean air action periods derived from the newly developed Inversed Emission Inventory for Chinese Air Quality (CAQIEI), *Earth Syst. Sci. Data* 16, 4351–4387 (2024).
29. Cao, T. et al. Rapid increase in spring ozone in the Pearl River Delta, China during 2013-2022. *npj Clim. Atmos. Sci.*7(1), 309 (2024).
30. Yan, X. et al. Declining $\Delta^{17}O$ of nitrate in the northeastern Tibetan Plateau reveals changing atmospheric oxidative capacity. *Earth Environ.* 7, 231 (2026).
31. Clapp, L. J., & Jenkin, M. E. Analysis of the relationship between ambient levels of O_3, NO_2 and NO as a function of NOx in the UK. *Environ.* 35, 6391–6405 (2001).
32. Dai, J. et al. The atmospheric oxidizing capacity in China–Part 1: Roles of different photochemical processes. *Chem. Phys.* 23(22), 14127-14158 (2023).
33. Dienhart, D. et al. Formaldehyde and hydroperoxide distribution around the Arabian Peninsula: Evaluation of EMAC model results with ship-based measurements. *Chem. Phys.* 23, 119–142 (2023).
34. Seinfeld, J. H., & Pandis, S. N. Atmospheric Chemistry and Physics: From Air Pollution to Climate Change, 3rd ed., Wiley, Hoboken, NJ (2016).
35. Atkinson, R. Atmospheric chemistry of VOCs and NOx. *Environ.* 34, 2063–2101 (2000).
36. Wang, N. et al. Climate-driven biogenic emissions alleviate the impact of human-made emission reductions on O_3 control in the Pearl River Delta region, southern China. *Chem. Phys.* 25, 8859–8870 (2025).
37. Hoesly, R. M. et al. Historical (1750–2014) anthropogenic emissions of reactive gases and aerosols from the Community Emissions Data System (CEDS). *Model Dev.* 11, 369–408 (2018).
38. van der Werf, G. R. et al. Global fire emissions estimates during 1997–2016. *Earth Syst. Sci. Data* 9, 697–720 (2017).
39. Zheng, B. et al. Global atmospheric carbon monoxide budget 2000–2017 inferred from multi-species atmospheric inversions. *Earth Syst. Sci. Data* 11, 1411–1436 (2019).
40. Jia, M. et al. Anthropogenic carbon monoxide emissions during 2014–2020 in China constrained by in situ ground observations, *Geophys. Res. Atmos.* 130, e2024JD042371 (2025).
41. Jia, M. et al. Rapid decline of carbon monoxide emissions in the Fenwei Plain in China during the Three-Year Action Plan on Defending the Blue Sky, *Environ. Manage.* 337, 117735 (2023).
42. Morichetti, M. et al. Comparison and evaluation of updates to WRF-Chem (v3.9) biogenic emissions using MEGAN, *Model Dev.* 15, 6311–6339 (2022).
43. Geng, G. et al. Efficacy of China's clean air actions to tackle PM_5 pollution between 2013 and 2020, *Nat. Geosci.* 17, 987–994 (2024).
44. Yang, H. et al. Weakened aerosol–radiation interaction exacerbating ozone pollution in eastern China since China's clean air actions, *Chem. Phys.*24(7), 4001-4015 (2024).

45. Ministry of Environmental Protection of the People's Republic of China. Notice on Effectively Carrying out Air Pollution Prevention and Control in the Coming Winter and Spring (MEE Doc. No. 101). http://www.mee.gov.cn/gkml/hbb/bgt/201611/t20161107_366960.htm (2016).
46. Ministry of Environmental Protection of the People's Republic of China. Notice on Effectively Carrying out Air Pollution Prevention and Control in the Coming Winter and Spring (MEE Doc. No. 97). http://www.mee.gov.cn/gkml/sthjbgw/qt/201510/t20151029_315831.htm (2015).
47. Ministry of Ecology and Environment of the People's Republic of China. Action Plan for the Comprehensive Control of Autumn and Winter Air Pollution in the Beijing-Tianjin-Hebei Region and Surrounding Areas (2018–2019) (MEE Doc. No. 100). http://www.mee.gov.cn/xxgk2018/xxgk/xxgk03/201809/t20180927_644173.html (2018).
48. The Paper. Expert interpretation of the current pollution sources in the Beijing–Tianjin–Hebei region: Industrial emissions increased significantly after the resumption of production. https://www.thepaper.cn/newsDetail_forward_2050414 (2018, last available on 5/30/2026).
49. Wang, Y. et al. Staggered-peak production is a mixed blessing in the control of particulate matter pollution. *npj Clim. Atmos. Sci.* 5, 99 (2022).
50. Changzhou Municipal Statistics Bureau. Monthly statistical report, available at: https://tjjyw.changzhou.gov.cn/cztjj/mbWeb_CZ.action, last available on 5/15/2026.
51. Weifang Municipal Statistics Bureau. Monthly statistical report, available at: https://tjj.weifang.gov.cn/tjjlist/?pid=trs13076263&catas=trs13076277, last available on 5/15/2026.
52. Zhengzhou Municipal Statistics Bureau. Monthly statistical report, available at: https://tjj.zhengzhou.gov.cn/tjyb/index.jhtml, last available on 5/15/2026.
53. Hangzhou Municipal Statistics Bureau. Monthly statistical report, available at: https://tjj.hangzhou.gov.cn/col/col1229279726/index.html, last available on 5/15/2026.
54. Hefei Municipal Statistics Bureau. Monthly data, available at: http://tjj.hefei.gov.cn/ydsj/ydjc/index.html, last available on 5/15/2026.
55. Beijing Municipal Statistics Bureau. Monthly statistical report, available at: https://tjj.beijing.gov.cn/tjsj_31433/yjdsj_31440/gy_31782/2026/index.html, last available on 5/15/2026.
56. Changsha Municipal Statistics Bureau. Monthly statistical report, available at: http://tjj.changsha.gov.cn/tjxx/tjsj/sjfb/, last available on 5/15/2026.
57. China Bureau of Statistics. Monthly data, available at: https://data.stats.gov.cn/dg/website/page.html#/pc/national/monthData, last available on 5/15/2026.
58. Zhang, Z. et al. The pollution control effect of the atmospheric environmental policy in autumn and winter: evidence from the daily data of Chinese cities. *Environ. Manage.* 343, 118164 (2023).
59. Huang, X. et al. Enhanced secondary pollution offset reduction of primary emissions during COVID-19 lockdown in China, *Sci. Rev.* 8, nwaa137 (2021).

60. Li, R., et al. Identifying the spatiotemporal variations in ozone formation regimes across China from 2005 to 2019 based on polynomial simulation and causality analysis, *Chem. Phys.* 21, 15631–15646 (2021).
61. Xue, L., et al. Critical transition of urban ozone formation regime in the North China Plain. *Sci. Rev.* 13(3), nwaf596 (2026).
62. Zhai, S., et al. Control of particulate nitrate air pollution in China. *Geosci.14*(6), 389-395 (2021).
63. Huang, X., et al. Characteristics of PM_5 pollution in Beijing after the improvement of air quality. *J. Environ. Sci.*100, 1-10 (2021).
64. Song, L. et al. Distinct evolutions of haze pollution from winter to the following spring over the North China Plain: role of the North Atlantic sea surface temperature anomalies. *Chem. Phys.* 22(3), 1669-1688 (2022).
65. Goldstein, A. H., & Galbally, I. E. Known and unexplored organic constituents in the earth's atmosphere. *Sci. Technol.*, 41(5), 1514-1521 (2007).
66. Xing, J., Wang, S. X., Jang, C., Zhu, Y., & Hao, J. M. Nonlinear response of ozone to precursor emission changes in China: a modeling study using response surface methodology. *Chem. Phys.*11(10), 5027-5044 (2011).
67. Holmes, C. D., Prather, M. J., Søvde, O. A., & Myhre, G. Future methane, hydroxyl, and their uncertainties: key climate and emission parameters for future predictions. *Chem. Phys.*13(1), 285-302 (2013).
68. Huang, X., et al. Effects of aerosol–radiation interaction on precipitation during biomass-burning season in East China. *Chem. Phys.*16(15), 10063-10082 (2016).
69. Huang, X., et al. Amplified transboundary transport of haze by aerosol–boundary layer interaction in China. *Geosci.*13(6), 428-434 (2020).
70. Ministry of Ecology and Environment of China. Ambient air — Automatic determination of nitrogen oxides — Chemiluminescence method (HJ 1043–2019), Beijing (2019).
71. Ministry of Ecology and Environment of China. Ambient air — Automatic determination of ozone — Chemiluminescence method (HJ 1225–2021), Beijing (2021).
72. Ministry of Ecology and Environment of China. Ambient air — Determination of ozone — Ultraviolet photometric method (HJ 590–2010), Beijing (2010).
73. Chance, K. OMI/Aura formaldehyde (HCHO) total column daily L3 weighted mean global 0.1° × 0.1° grid, NASA Goddard Earth Sciences Data and Information Services Center (GES DISC) (2019).
74. Pisso, I. et al. The Lagrangian particle dispersion model FLEXPART version 10.4, *Model Dev.* 12, 4955–4997 (2019).
75. Thompson, R. L., & Stohl, A. FLEXINVERT: An atmospheric Bayesian inversion framework for determining surface fluxes of trace species using an optimized grid, *Model Dev.* 7, 2223–2242 (2014).

76. Zaveri, R. A., & Peters, L. K. A new lumped structure photochemical mechanism for large-scale applications, *Geophys. Res. Atmos.* 104, 30387–30415 (1999).
77. Zaveri, R. A., Easter, R. C., Fast, J. D., & Peters, L. K. Model for Simulating Aerosol Interactions and Chemistry (MOSAIC), *Geophys. Res. Atmos.* 113, D13204 (2008).
78. Noh, Y., Cheon, W. G., Hong, S. Y., & Raasch, S. Improvement of the K-profile model for the planetary boundary layer based on large eddy simulation data, *-Layer Meteorol.* 107, 401–427 (2003).
79. Grell, G. A., & Freitas, S. R. A scale- and aerosol-aware stochastic convective parameterization for weather and air quality modeling, *Chem. Phys.* 14, 5233–5250 (2014).
80. Lin, Y. L., Farley, R. D., & Orville, H. D. Bulk parameterization of the snow field in a cloud model, *Clim. Appl. Meteorol.* 22, 1065–1092 (1983).
81. Mlawer, E. J., Taubman, S. J., Brown, P. D., Iacono, M. J., & Clough, S. A. Radiative transfer for inhomogeneous atmospheres: RRTM, *Geophys. Res.* 102, 16663–16682 (1997).
82. Iacono, M. J. et al. Radiative forcing by long-lived greenhouse gases: Calculations with the AER radiative transfer models, *Geophys. Res. Atmos.* 113, D13103 (2008).
83. Monin, A. S., & Obukhov, A. M. Basic laws of turbulent mixing in the surface layer of the atmosphere, *Akad. Nauk SSSR, Geophyiz. Inst.* 24, 163–187 (1954).
84. Chen, F. et al. Modeling of land surface evaporation by four schemes and comparison with FIFE observations, *Geophys. Res. Atmos.* 101, 7251–7268 (1996).
85. Ek, M. B. et al. Implementation of Noah land surface model advances in the NCEP operational mesoscale Eta model, *Geophys. Res.* 108, 8851 (2003).
86. Stauffer, D. R., & Seaman, N. L. Multiscale four-dimensional data assimilation, *Appl. Meteorol.* 33, 416–434 (1994).
87. Deng, A. et al. Update on WRF-ARW end-to-end multiscale FDDA system, *Proceedings of the 10th WRF Users' Workshop*, NCAR, Boulder, CO (2009).
88. National Centers for Environmental Prediction/National Weather Service/NOAA. NCEP ADP global upper air observational weather data, NCAR Research Data Archive (2004).

Figures

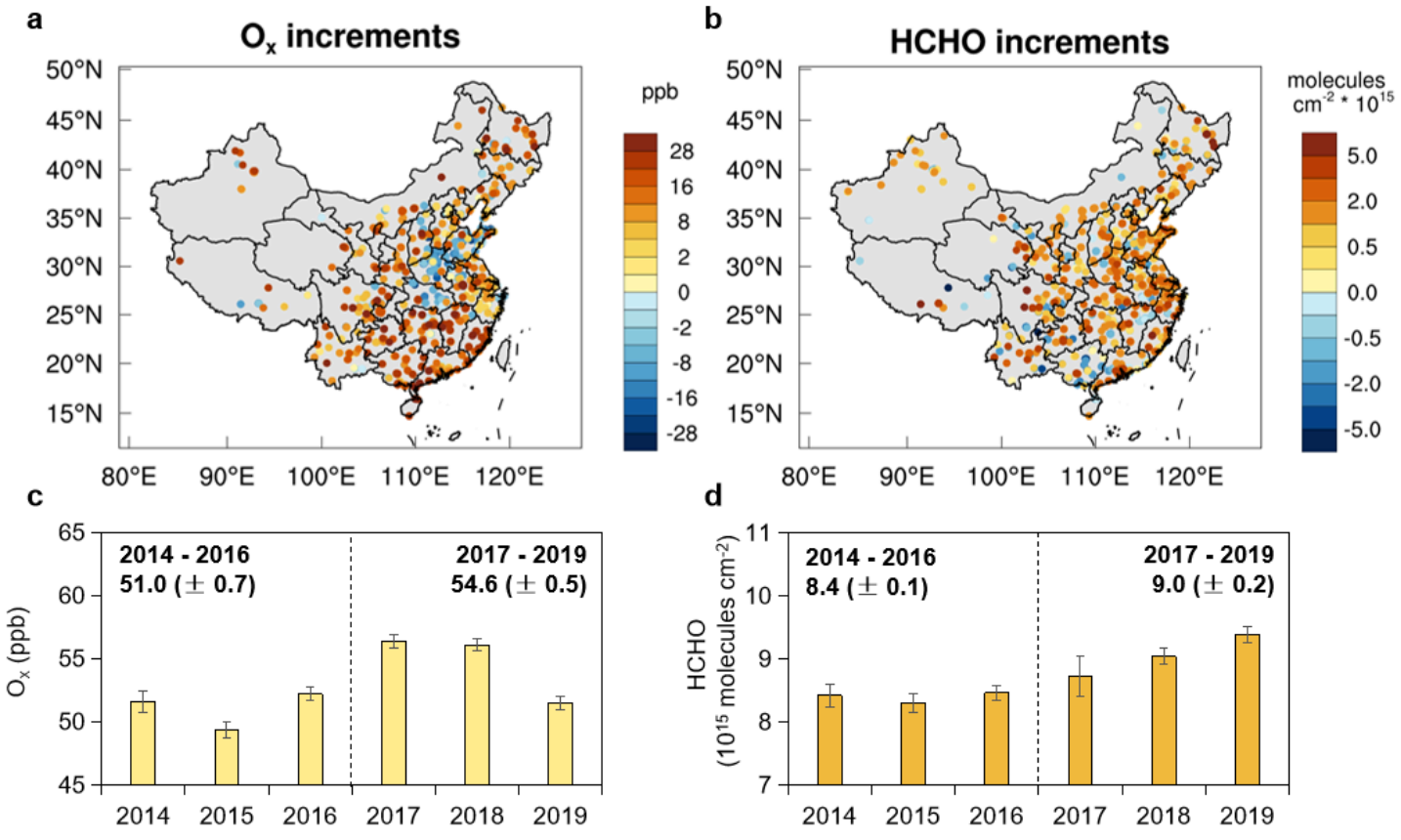


Figure 1

Spatiotemporal changes of ground-based atmospheric oxidation indicator Ox concentrations and satellite-based HCHO vertical column densities (VCD) in spring from 2014 to 2019. (a - b) Spatial distributions of the changes in **(a)** Ox concentrations and **(b)** HCHO VCD in the spring of 2017-2019 compared to the spring of 2014-2016; **(c - d)** Interannual variations of **(c)** Ox concentrations and **(d)** HCHO VCD in spring from 2014 to 2019. Error bars in **(c)** and **(d)** represent 95% confidence intervals.

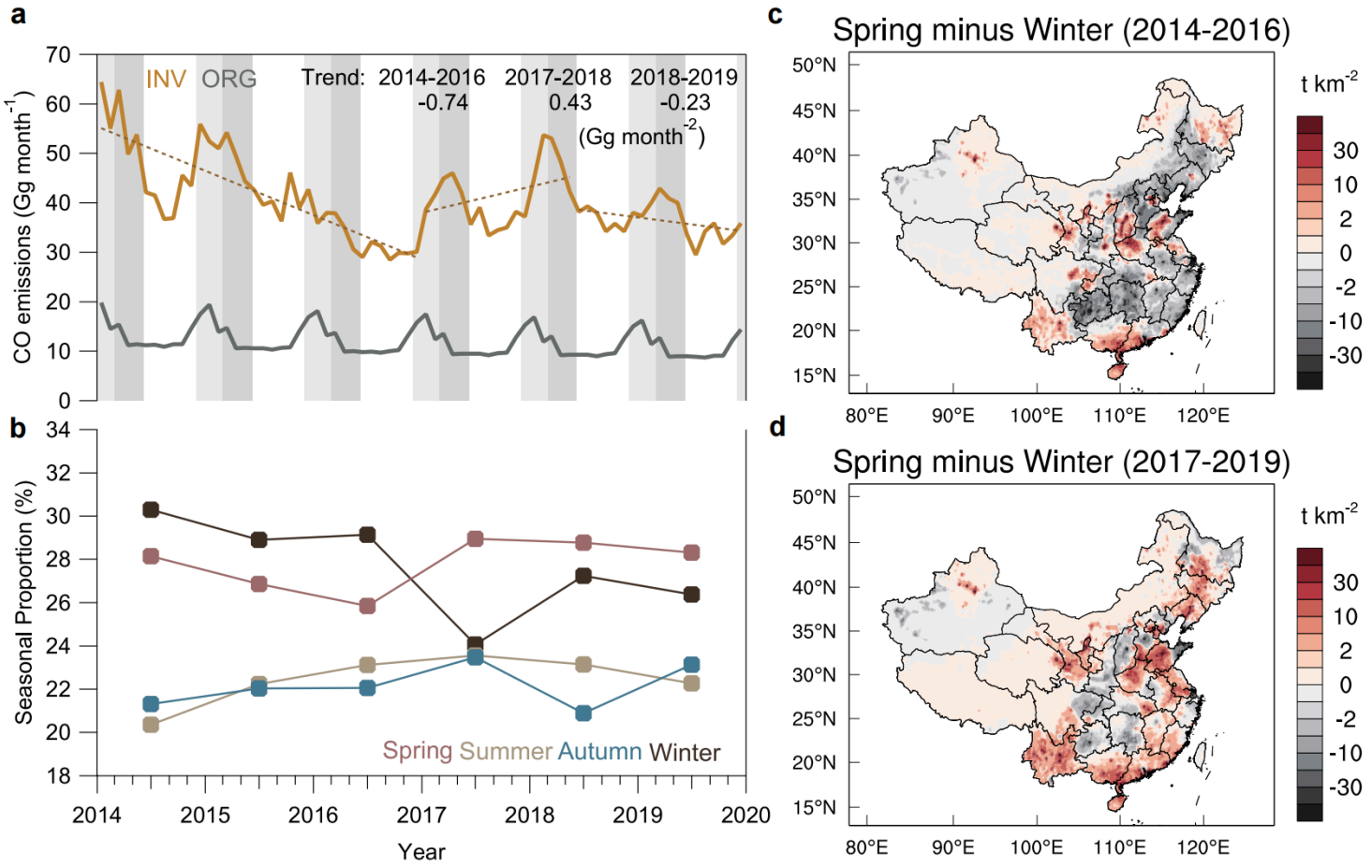


Figure 2

Spatiotemporal changes of anthropogenic CO emissions from 2014 to 2019. (a) Monthly anthropogenic CO emissions from the bottom-up emission inventory (ORG) and the inverted emissions (INV), with light gray shading indicating the spring period and dark gray shading indicating the winter period; **(b)** Seasonal proportion of the inverted emissions; **(c - d)** The differences in anthropogenic CO emissions between spring and winter (spring minus winter) during 2014–2016 **(c)** and 2017–2019 **(d)**. After 2017, the springtime anthropogenic CO emissions exceeded the winter emissions.

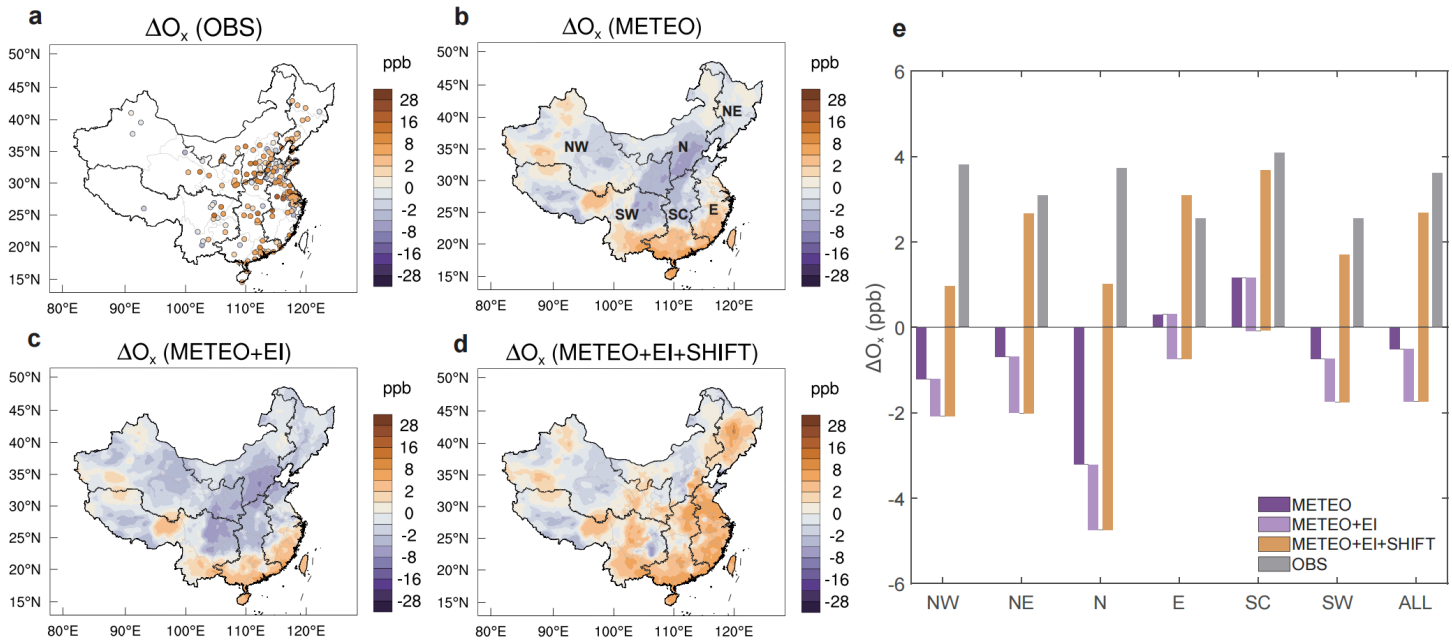


Figure 3

Contributions of changes in meteorology and in emissions with and without seasonal emission shifts to ΔOx from spring 2014 to spring 2017 in China. (a) Observed changes in city-averaged springtime O_x concentrations; **(b)** The contribution of meteorological change only; **(c)** The contribution of changes in both meteorological conditions and emissions without seasonal shift; **(d)** The contribution of changes in both meteorological conditions and emissions with seasonal shift; **(e)** Statistical results of city-averaged ΔO_x concentrations, where NW, NE, N, E, SC, SW, and ALL denote Northwest China, Northeast China, North China, East China, South-Central China, Southwest China, and nationwide, respectively.

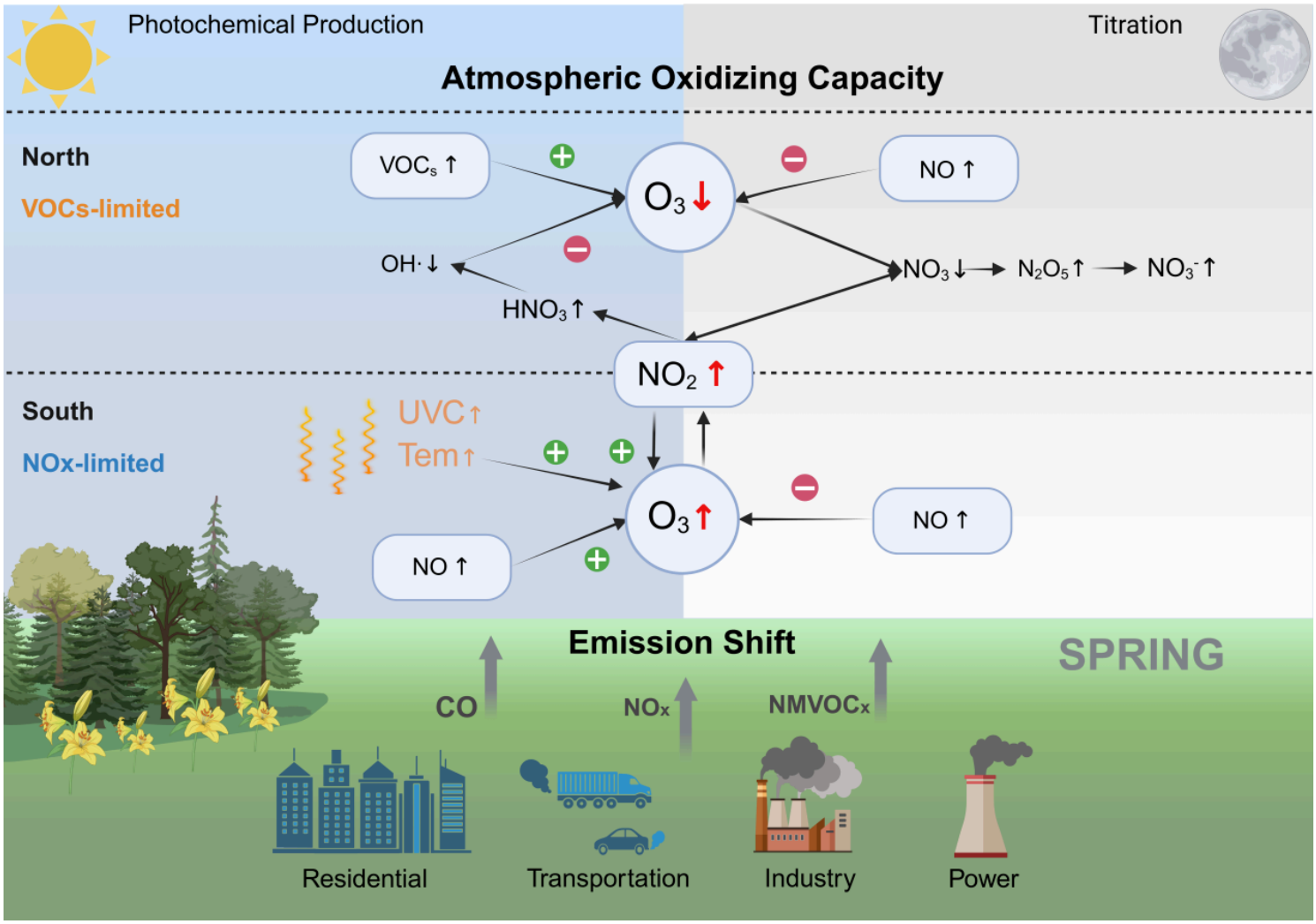


Figure 4

Nonlinear chemistry mechanisms of AOC following springtime emission shifts. The impacts of enhanced springtime direct emissions, including CO, NO_x, and non-methane volatile organic compounds (NMVOCs), on AOC exhibit pronounced diurnal and north-south contrasts, leading to substantial O_3 increases in NO_x-limited regions and enhanced nitrate formation in VOC-limited regions.

Supplementary Files

This is a list of supplementary files associated with this preprint. Click to download.

- Supplementarysubmitted.docx